Hybrid Electromagnetic Reconstruction of Multiple 2-D Subsurface Inhomogeneous Objects Based on FRTM and FEBI-LM Methods Enhanced by Domain Decomposition

Jiawen Li, Qi Qiang Liu, *Member, IEEE*, Zhen Guan, and Feng Han, *Senior Member, IEEE*

***Abstract*—This article presents a hybrid method to reconstruct multiple 2-D inhomogeneous objects straddling multiple subsurface planar layers and segmented into multiple subdomains. In the forward electromagnetic (EM) scattering computation, the finite-element boundary integral (FEBI) method is employed to simultaneously solve for the total electric fields inside the multiple subdomains and the equivalent current on their boundaries, which are connected with each other by the 2-D layered-medium dyadic Green's functions (LMDGFs). The scattered fields at the receiver array are then obtained by multiplying the boundary current with radiation matrices. The EM reconstruction is implemented in two steps. First, the frequency-domain reverse time migration (FRTM) combined with a level set of the indicator function and the *K*-means clustering is used to determine the approximate rectangular boundary for each full-wave inversion (FWI) subdomain. Second, the sensitivity matrix of the measured scattered electric fields with respect to the dielectric parameters inside all rectangular subdomains is assembled. The Levenberg–Marquardt (LM) method is then used to fulfill the multidomain EM FWI by iteratively calling the FEBI forward solver. Numerical experiments are carried out to compare the implementation cost and efficiency of the forward FEBI solver and the inverse FEBI-LM solver with and without domain decomposition (DD).**

***Index Terms*—Domain decomposition (DD), electromagnetic (EM) reconstruction, finite-element boundary integral (FEBI) method, Levenberg–Marquardt (LM) method.**

I. Introduction

SUBSURFACE reconstruction by electromagnetic (EM) waves has been drawing more and more attention in recent years due to its wide applications in both military and civil areas such as land mine detection [1], buried pipe inspection [2], pavement crack surveys [3], and unexploded ordinance characterization [4].

Based on the information content of the unknown targets obtained in the reconstruction [5], the commonly used EM reconstruction approaches can be categorized into qualitative methods and quantitative ones. Qualitative methods mainly include migration, sampling, and tomography [6]. For example, the reverse time migration (RTM) widely adopted in subsurface detection by a ground penetrating radar (GPR) [7] is realized by solving the two-way EM wave equation and invoking the cross correlation imaging condition [8]. The modified frequency-domain RTM (FRTM) can overcome the high-cost defect of the traditional RTM [9] by computing the horizontally layered-medium dyadic Green's functions (LMDGFs) in advance [10]. The linear sampling method (LSM) achieves the scatterer support reconstruction by determining the gain matching relationship between the scattered field data recorded at the receiver array and Green's functions corresponding to a series of fictitious source points in the imaging domain [11], [12]. In diffraction tomography, the EM scattering equation is usually linearized by the Born or Rytov approximation [13]. Consequently, the images of electrically small objects placed inside a stratified medium can be directly obtained without iterations [14]. The backpropagation (BP) algorithm used in reflection tomography obtains the scatterer image by mapping the measured scattered fields back to the fictitious induced current in the imaging domain [15], [16]. Although these qualitative methods can reconstruct unknown objects in a relatively fast fashion, only the general locations and rough shapes are retrieved. In particular, for the subsurface reconstruction, when the imaging domain is only illuminated in the topside, both LSM and BP only obtain severely distorted shapes and blurry boundaries of the buried objects [17], [18].

The quantitative reconstruction, which is always realized by EM full-wave inversion (FWI), is able to retrieve both the accurate shapes and dielectric parameters of the unknown subsurface objects. The commonly used EM FWI is formulated using the volume integral equations (VIEs) in which the equivalent current and EM fields in all the discretized pixels are interconnected by Green's functions [19]. In order to lower the computational cost of the forward scattering, researchers use the fast Fourier transform (FFT) to accelerate the integration of the multiplication of the equivalent current

Received 19 March 2025; revised 23 August 2025; accepted 10 September 2025. This work was supported by the National Natural Science Foundation of China under Grant 62461005 and Grant 62271428. *(Corresponding author: Feng Han.)*

Jiawen Li is with the Guangxi Key Laboratory of Brain-inspired Computing and Intelligent Chips, School of Electronic and Information Engineering, Guangxi Normal University, Guilin 541004, China, and also with the Key Laboratory of Integrated Circuits and Microsystems, Education Department of Guangxi Zhuang Autonomous Region, Guangxi Normal University, Guilin 541004, China (e-mail: jiawenli@mailbox.gxnu.edu.cn).

Qi Qiang Liu is with the School of Electronics and Information Engineering, Hangzhou Dianzi University, Hangzhou 310018, China (e-mail: liuqiqiang@hdu.edu.cn).

Zhen Guan is with the Great Bay Institute for Advanced Study, Dongguan 523000, China, also with the School of Computing and Information Technology, Great Bay University, Dongguan, Guangdong 523000, China, and also with the School of Information Science and Technology, University of Science and Technology of China, Hefei 230027, China (e-mail: zguan@gbu.edu.cn).

Feng Han is with the School of Computing and Information Technology, Great Bay University, Dongguan, Guangdong 523000, China, and also with the Institute of Electromagnetics and Acoustics, Xiamen University, Xiamen 361005, China (e-mail: feng.han@gbu.edu.cn; feng.han@xmu.edu.cn).

Digital Object Identifier 10.1109/TAP.2025.3611311

0018-926X © 2025 IEEE. All rights reserved, including rights for text and data mining, and training of artificial intelligence and similar technologies. Personal use is permitted, but republication/redistribution requires IEEE permission.
See https://www.ieee.org/publications/rights/index.html for more information.

IEEE Proof

and Green's functions, which can be treated as convolution for a homogeneous [20] or a planarly stratified [21] background medium. Based on this fast forward scattering algorithm, a series of FWI methods such as contrast source inversion (CSI) and variational Born iterative method (VBIM) have been developed to reconstruct subsurface 3-D isotropic objects [22] or anisotropic ones [23]. Unfortunately, these inversion methods must sustain unaffordable computational cost when the subsurface scatterers straddle multiple layers or a rough surface is present [24]. The root reason is that the shift-invariance property of Green's functions is disrupted, and thus, the FFT acceleration fails in the forward scattering computation. Although some direct forward solvers can avoid the FFT acceleration of the multiplication of matrices and vectors, they are unsuitable for our subsurface reconstruction problem. For example, the low-rank-based $\mathcal{H}$ matrices algorithm [25] realizes the fast solution of the discretized integral equations by approximating the original dense impedance matrix into a sparse one through finding some subblocks in it that can be estimated by some low-rank matrices. However, such an approximation requires asymptotically smooth kernels [26]. The EM wave reflection in the layered background interface actually deteriorates the smoothness of the Green's function kernel, which will suppress the superiority of the $\mathcal{H}$ matrices algorithm. Although the hierarchical $\mathcal{H}^2$ matrices method [27] still can keep the low-rank advantage for oscillatory kernels, it usually requires more involved computation [26]. Since the implementation of FWI usually includes numerous forward scattering computation, applying the $\mathcal{H}^2$ matrices method may incur a remarkable additional cost.

The EM FWI based on differential equations (DEs) can completely overcome the heavy dependence on fast algorithms for forward scattering computation based on VIEs since the local EM fields are described by differential-form Maxwell equations or the Helmholtz equations, and thus, Green's functions become unnecessary. Previous research results indicate that the conventional DE-based numerical approaches such as the finite-element method (FEM) can be directly used in EM FWI, e.g., geophysical exploration [28] as long as absorbing boundary conditions are imposed on the inversion domain. In our previous work [29], we use the FEM to compute EM fields scattered from 2-D subsurface objects straddling multiple planar layers but with a radiation boundary condition (RBC) to truncate the computational domain. The equivalent current on the radiation boundary is formulated by the 1-D boundary integral (BI) equation and solved by the traditional method of moments (MoMs). This finite-element BI (FEBI) method is further combined with the Levenberg–Marquardt (LM) method to reconstruct 2-D inhomogeneous objects straddling multiple subsurface layers. The current work is the extension of [29]. The motivation is to reconstruct multiple subsurface 2-D objects positioned far from each other at a low cost by introducing domain decomposition (DD). Specifically speaking, the whole computational domain is decomposed into several independent subdomains in which the 2-D scatterers are placed. Each subdomain is enclosed by a smooth radiation boundary and the FEBI method is adopted to solve for the EM fields inside it. The EM fields and equivalent current

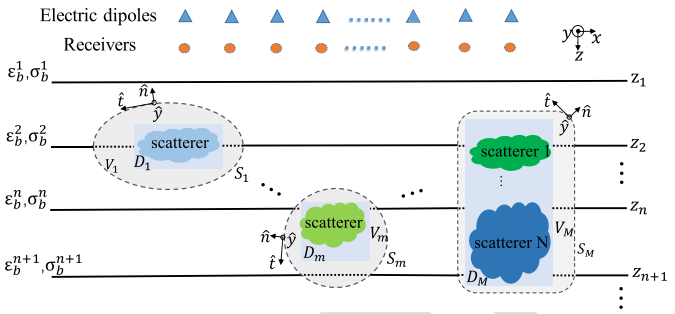

Fig. 1. Multiple 2-D inhomogeneous scatterers straddling multiple subsurface planar layers and enclosed by multiple smooth boundaries are illuminated by a series of electric dipoles. The FEBI method with the DD is adopted to compute the scattered fields at the receiver array. In the inversion, the FRTM provides the a priori information for the FEBI-LM implementation.

at all the subdomain boundaries are linked by LMDGFs. The state equation is thus formulated with DD and the total EM fields at all these boundaries are obtained. They are multiplied with radiation matrices to compute the scattered EM fields at the receiver array [29]. In the reconstruction, the qualitative method FRTM combined with a level set of the indicator function and the K-means clustering is first used to determine the boundaries of multiple subdomains, and then, the FEBI-LM is implemented to invert dielectric parameters of scatterers enclosed inside them. One should note that, although the adaptive cross approximation (ACA) algorithm also saves computation time and memory cost in multidomain EM scattering problems [30], it cannot be used for the FWI of multiple subsurface objects since the matrix approximation by a series of vector products in the forward scattering computation may lead to accumulated errors in the inverse iterations. This phenomenon will become more severe when the subdomains are closer to each other.

The rest of this article is organized as follows. In Section II, the formulas for the 2-D FEBI method with DD are first derived based on the formulas given in [29]. Then, the 2-D FRTM is briefly mentioned. The level set of the indicator function and the K-means clustering used to determine the multiple rectangular FWI regions based on the FRTM image are described. Finally, the assembly of the sensitivity matrix for the FEBI-LM method with DD is discussed in detail. In Sections III and IV, a forward scattering example and two FWI examples are, respectively, given to validate the reliability and computation efficiency of the FEBI method with DD and the FEBI-LM method with DD assisted by FRTM. In Section V, the conclusion and summary are presented.

II. Methods

As shown in Fig. 1, several inhomogeneous scatterers are separately placed inside the computational subdomains $V_1, \ldots, V_M$, which straddle multiple subsurface planar layers and are wrapped by the smooth boundaries $S_1, \ldots, S_M$. This EM scattering configuration is the extension of that shown in [29, Fig. 1(a)] but with the DD introduced. The forward scattering computation for the mth subdomain is fulfilled by FEM implemented inside V_m and by BI on the boundary S_m. However, the FWI is fulfilled by LM implemented in the

IEEE Proof

rectangular region D_m. In the following, we will detailedly discuss the assembly of the system matrix for the FEBI method with DD, the implementation of FRTM to obtain the approximate locations of the subsurface objects, the level-set method to determine the multiple rectangular regions for FWI, and the assembly of the sensitivity matrix for FWI with DD.

A. Assembly of the System Matrix for 2-D FEBI With DD

We make several assumptions before the derivation. First, only the transverse electric (TE) mode is considered in this work. All the mathematical formulas presented in this work can be referred to those given in [29] for the TE mode. Second, the whole region is divided into M subdomains. Each subdomain and its smooth boundary are discretized using the same strategy adopted in [29]. Therefore, the mth subdomain V_m is discretized into several quadrilateral elements with N_i^m nodes and its boundary S_m is divided into N_b^m arcs. Third, there are N_T transmitters and N_R receivers placed in the first layer, which is air. The discretized algebraic state equation for FEBI with DD can be compactly written as follows:

$$\mathbf{Z}\mathbf{e} = \mathbf{V} \tag{1}$$

where

$$\mathbf{Z} = \begin{bmatrix} \mathbf{Z}^{1,1} & \cdots & \mathbf{Z}^{1,m} & \cdots & \mathbf{Z}^{1,M} \\ \vdots & \ddots & & & \vdots \\ \mathbf{Z}^{m,1} & & \mathbf{Z}^{m,m} & & \mathbf{Z}^{m,M} \\ \vdots & & & \ddots & \vdots \\ \mathbf{Z}^{M,1} & \cdots & \mathbf{Z}^{M,m} & \cdots & \mathbf{Z}^{M,M} \end{bmatrix} \tag{2a}$$

$$\mathbf{e} = \left[\mathbf{e}^1 \cdots \mathbf{e}^m \cdots \mathbf{e}^M\right]^T \tag{2b}$$

$$\mathbf{V} = \left[\mathbf{V}^1 \cdots \mathbf{V}^m \cdots \mathbf{V}^M\right]^T \tag{2c}$$

in which superscript T denotes the matrix transpose by block and superscript m denotes the mth subdomain. A submatrix in the diagonal line of (2a) has the same structure as the $\mathbf{Z}^h$ matrix in [29, eq. (5)] but is only constructed for the FEBI implementation inside the mth subdomain shown in Fig. 1. The nondiagonal submatrices in (2a) represent the mutual coupling among $S_1, \ldots, S_M$. Let us take $\mathbf{Z}^{m,m}$ and $\mathbf{Z}^{m,1}$ as examples. Since the discretization strategy used here is the same as that adopted in [29], they have the dimensions of $(N_i^m + 2N_b^m) \times (N_i^m + 2N_b^m)$ and $(N_i^m + 2N_b^m) \times (N_i^1 + 2N_b^1)$. By referring to [29, eq. (5)], we can construct them as follows:

$$\mathbf{Z}^{m,m} = \begin{bmatrix} \mathbf{Z}_{ii}^m & \mathbf{Z}_{ib}^m & \mathbf{0} \\ \mathbf{Z}_{bi}^m & \mathbf{Z}_{bb}^m & \mathbf{Z}_S^m \\ \mathbf{0} & \mathbf{Z}_M^{m,m} & \mathbf{Z}_J^{m,m} \end{bmatrix} \tag{3a}$$

$$\mathbf{Z}^{m,1} = \begin{bmatrix} \mathbf{0} & \mathbf{0} & \mathbf{0} \\ \mathbf{0} & \mathbf{0} & \mathbf{0} \\ \mathbf{0} & \mathbf{Z}_M^{m,1} & \mathbf{Z}_J^{m,1} \end{bmatrix} \tag{3b}$$

in which the dimensions of each submatrix in (3a) have been discussed in [29, Sec. II]. In (3b), $\mathbf{Z}_M^{m,1} \in \mathbb{C}^{N_b^m \times N_b^1}$ represents the coupling from the equivalent magnetic current on S_1 to the electric fields on S_m, while $\mathbf{Z}_J^{m,1} \in \mathbb{C}^{N_b^m \times N_b^1}$ represents the coupling from the equivalent electric current on S_1 to the electric fields on S_m. The detailed assembly of each submatrix of $\mathbf{Z}^{m,m}$ and $\mathbf{Z}^{m,1}$ is given in (A1) in the Appendix. One should note that subscript M in (3) denotes the magnetic current instead of the index of S_M. In a similar way, by referring to [29, eq. (5)], we can construct the submatrix $\mathbf{e}^m \in \mathbb{C}^{(N_i^m+2N_b^m)\times N_T}$ in (2b) and the submatrix $\mathbf{V}^m \in \mathbb{C}^{(N_i^m+2N_b^m)\times N_T}$ in (2c) as follows:

$$\mathbf{e}^m = \begin{bmatrix} \mathbf{e}_i^m \\ \mathbf{e}_b^m \\ \overline{\mathbf{J}}_b^m \end{bmatrix}, \quad \mathbf{V}^m = \begin{bmatrix} \mathbf{0} \\ \mathbf{0} \\ \mathbf{V}_S^m \end{bmatrix} \tag{4}$$

in which $\mathbf{e}^m$ is the unknown coefficient matrix and $\mathbf{V}^m$ is the source matrix whose computation is given in (A2) in the Appendix. Finally, it is worth mentioning that the system matrix $\mathbf{Z}$ in (1) has the dimensions of $\Sigma_{m=1}^M (N_i^m + 2N_b^m) \times \Sigma_{m=1}^M (N_i^m + 2N_b^m)$, the unknown matrix $\mathbf{e}$ has the dimensions of $\Sigma_{m=1}^M (N_i^m + 2N_b^m) \times N_T$, and $\mathbf{V}$ has the same dimensions. Once $\mathbf{e}$ is solved for from (1), the scattered EM fields at the receiver array can be obtained by multiplying the radiation matrix by $\mathbf{e}$. They are written as follows:

$$\mathbf{E}_y^{sct} = \mathbf{R}^{E_y}\mathbf{e} = \left[\mathbf{R}^{E_y,1} \cdots \mathbf{R}^{E_y,m} \cdots \mathbf{R}^{E_y,M}\right]\mathbf{e} \tag{5a}$$

$$\mathbf{H}_x^{sct} = \mathbf{R}^{H_x}\mathbf{e} = \left[\mathbf{R}^{H_x,1} \cdots \mathbf{R}^{H_x,m} \cdots \mathbf{R}^{H_x,M}\right]\mathbf{e} \tag{5b}$$

$$\mathbf{H}_z^{sct} = \mathbf{R}^{H_z}\mathbf{e} = \left[\mathbf{R}^{H_z,1} \cdots \mathbf{R}^{H_z,m} \cdots \mathbf{R}^{H_z,M}\right]\mathbf{e} \tag{5c}$$

in which $\mathbf{R}^{E_y,m} = \left[\mathbf{0} \quad \mathbf{R}_M^{E_y,m} \quad \mathbf{R}_J^{E_y,m}\right]$, $\mathbf{R}^{H_x,m} = \left[\mathbf{0} \quad \mathbf{R}_M^{H_x,m} \quad \mathbf{R}_J^{H_x,m}\right]$, and $\mathbf{R}^{H_z,m} = \left[\mathbf{0} \quad \mathbf{R}_M^{H_z,m} \quad \mathbf{R}_J^{H_z,m}\right]$. The detailed assemblies of these submatrices are given in (A3) in the Appendix. In addition, the overall radiation matrices $\mathbf{R}^{E_y}$, $\mathbf{R}^{H_x}$, and $\mathbf{R}^{H_z}$ have the same dimensions of $N_R \times \Sigma_{m=1}^M (N_i^m + 2N_b^m)$.

B. Implementation of 2-D FRTM

Because the boundary of each subdomain shown in Fig. 1 in the FWI is unknown, a qualitative method is necessary to find the approximate locations of the subsurface scatterers at first. Since both LSM and BP are only able to acquire blurry top and bottom boundaries of the buried objects when they are illuminated in the topside [17], [18], we choose RTM as the qualitative method. In a planarly layered background, FRTM shows the obvious superiority of computational cost over the traditional RTM for imaging the subsurface objects [10]. Its imaging condition is realized by integrating the wavefield data over the whole frequency band

$$I(\boldsymbol{\rho}) = \frac{1}{2\pi}\int_{-\infty}^{+\infty} U_r(\boldsymbol{\rho},\omega)\, U_s(\boldsymbol{\rho},\omega)\, e^{j\omega T} dw \tag{6}$$

where $\boldsymbol{\rho} = \hat{x}x + \hat{z}z$ is the spatial sampling position in the 2-D imaging domain, T is the time window of the recorded GPR traces, ω is the operation angular frequency, $U_s(\boldsymbol{\rho},\omega)$ is the Fourier spectrum of the source wavefield, and $U_r(\boldsymbol{\rho},\omega)$ is the spectrum of the receiver wavefield. They are obtained by multiplying the 2-D layered-medium Green's function with the spectra of the source wavelet and receiver signals [31], respectively,

$$U_s(\boldsymbol{\rho},\omega) = g\left(\boldsymbol{\rho},\boldsymbol{\rho}_s,\omega\right) \cdot S\left(\boldsymbol{\rho}_s,\omega\right) \tag{7a}$$

$$U_r(\boldsymbol{\rho},\omega) = g\left(\boldsymbol{\rho},\boldsymbol{\rho}_r,\omega\right) \cdot R^*\left(\boldsymbol{\rho}_r,\omega\right) e^{-j\omega T} \tag{7b}$$

IEEE Proof

where g is the Green's function, S is the spectrum of the source waveform transmitted from $\boldsymbol{\rho}_s$, and R is the spectrum of the recorded signal sampled at $\boldsymbol{\rho}_r$. For the 2-D TE mode, the layered-medium g actually is the $\hat{y}\hat{y}$-component of the 3-D LMDGF $\overline{\overline{\mathbf{G}}}_{\mathbf{EJ}}$ whose evaluation can be found in [32, eq. (28)] and [33, eqs. (21)–(24)]. Finally, we want to emphasize that, compared with the detailed FRTM algorithm given in [10], the only difference in this work is that 2-D transmitters and receivers are used.

C. Determination of the 2-D Rectangular Boundary For Each FWI Subdomain

Because the FRTM discussed in Section II-B only provides the approximate locations of the subsurface objects [10], it is necessary to implement some new algorithms to determine the specific rectangular boundary for each subdomain D_m shown in Fig. 1. In this work, we apply the level set to an indicator function built for a normalized image [34] and then use the K-means clustering [35] to finally determine the rectangular boundary. The details are listed in the following.

1) Use (6) to compute the image $I^{(1)}$ when the unknown subsurface objects are present and the image $I_b^{(1)}$ when they are absent. Therefore, $I_b^{(1)}$ is the theoretical image of the original layered background since the layer interface position is known.
2) Compensate the image intensity attenuation of both $I^{(1)}$ and $I_b^{(1)}$ caused by the EM wave propagation inside the conductive subsurface region by multiplying them with the same varying factor, which increases with the depth z. The compensation is mathematically formulated as follows:

$$I^{(2)} = I^{(1)} \times \alpha \left[\sqrt{z} e^{|k_i^n| z} \right]^2 \tag{8a}$$

$$I_b^{(2)} = I_b^{(1)} \times \alpha \left[\sqrt{z} e^{|k_i^n| z} \right]^2 \tag{8b}$$

where α is an empirical coefficient, k_i^n is the imaginary part of the wavenumber for the center frequency of the source wavelet propagation inside the nth subsurface layer, and the squared power corresponds to the multiplication of U_s and U_r in (6). Note that the compensation factor in (8) comes from the large argument approximation of the 2-D Green's function (zeroth-order Hankel function of the second kind), which is proportional to $\sqrt{(2/\pi k \rho)} e^{-jk\rho}$ [36]. In addition, the compensation is not implemented for the subsurface regions $0.5\lambda_{\mathrm{FRTM}}$ above and $2.0\lambda_{\mathrm{FRTM}}$ beneath a layer interface. Here, the wavelength λ_{FRTM} is computed based on the center frequency of the source wavelet and corresponding layer parameters. This circumvention is reasonable since a layer interface itself is known but generates a strong disturbance to scatterer images.
3) Subtract the compensated background image $I_b^{(2)}$ from the compensated overall image $I^{(2)}$ using

$$I^{(3)} = I^{(2)} - I_b^{(2)} \tag{9}$$

where $I^{(3)}$ only includes the compensated image of the unknown subsurface objects.
4) Refer to [34, eq. (5)], directly use the gray value difference to avoid the logarithm of zero, and construct the indicator function for a normalized image as follows:

$$I^{(4)}(i,k) = \frac{\left|I^{(3)}(i,k)\right| - \left|I^{(3)}\right|_{\min}}{\left|I^{(3)}\right|_{\max} - \left|I^{(3)}\right|_{\min}} \tag{10}$$

where i and k are the indices of the image pixels in the $\hat{x}$-direction and $\hat{z}$-direction, respectively; $|I^{(3)}|_{\min}$ is the minimum value of absolute values of $I^{(3)}$ in all the pixels; and $|I^{(3)}|_{\max}$ is the maximum value of absolute values of $I^{(3)}$ in all the pixels.
5) Convert the indicator function $I^{(4)}$ to a binary image by

$$I^{(5)}(i,k) = \begin{cases} 1, & \text{if } I^{(4)}(i,k) \geq \beta \\ 0, & \text{if } I^{(4)}(i,k) < \beta \end{cases} \tag{11}$$

where β is an empirical-level threshold. The purpose of this level set is to filter out the weak clutter in the FRTM image caused by noise and explicitly determine the "scatterer" or "background" for a certain pixel in the normalized image.
6) Segment the binary image $I^{(5)}$ into a series of larger square blocks, each of which approximately has the size of $0.5\lambda_0 \times 0.5\lambda_0$ and contains N_0 pixels. Here, λ_0 is the wavelength for the center frequency of the source wavelet in the free space. Denote the collections of the indices i and k for the pixels located inside the bth square block as $\mathcal{I}_b$ and $\mathcal{K}_b$, respectively, and desensitize the binary image $I^{(5)}$ by

$$I^{(6)}(i,k) = \begin{cases} 1, & \text{if } \frac{1}{N_0} \times \sum\limits_{\substack{i \in \mathcal{I}_b \\ k \in \mathcal{K}_b}} I^{(5)}(i,k) \geq \gamma \\ 0, & \text{if } \frac{1}{N_0} \times \sum\limits_{\substack{i \in \mathcal{I}_b \\ k \in \mathcal{K}_b}} I^{(5)}(i,k) < \gamma \end{cases} \tag{12}$$

where γ is an empirical-level threshold. The purpose of this level set is to filter out the strong and large clutters in the FRTM image caused by noise or interferences between layer boundaries and scatterers or among different scatterers.
7) Estimate the isolated scatterer number based on $I^{(6)}$ and the basic features of an RTM image, e.g., the curved upper and lower boundaries. Implement the K-means clustering to group the "scatterer" pixels in $I^{(6)}$.
8) Determine the boundary of each rectangular subdomain D_m based on the outermost pixels of each group in four directions, usually with an extension of $0.5\lambda_{\mathrm{FRTM}}$. Merge partially overlapped rectangular subdomains or isolated upper boundary and lower boundary subdomains.

D. Assembly of the Sensitivity Matrix for 2-D FEBI-LM With DD

Because the rectangular subdomains $D_1, \ldots, D_M$ determined by the algorithm given in Section II-C in which the EM FWI will be performed keep at least one quadrilateral element away from the boundaries $S_1, \ldots, S_M$ [29], the sensitivity matrix for FEBI-LM is only related to the diagonal submatrices $\mathbf{Z}^{1,1}, \ldots, \mathbf{Z}^{M,M}$ in (2a). For convenience to continue the derivation, we make several assumptions here. First, to avoid

IEEE Proof

confusion, we use the subscript l to replace the subscript m of the x_m in [29, eqs. (17)–(19)]. Therefore, x_l^m in the following derivation denotes the dielectric model parameter, i.e., the complex relative permittivity, in the lth discrete quadrilateral element of the subdomain D_m. Second, all the nodes inside all M subdomains are numbered sequentially from V_1 to V_M. Specifically speaking, the order is that all the nodes inside V_1 are numbered first, and then, those inside V_2 are numbered following the index for the last node in V_1. This procedure continues until all the nodes inside V_M are numbered. Third, the four vertices of the lth quadrilateral element in all the discrete nodes of the subdomain V_m are numbered as p_1^m, p_2^m, p_3^m, and p_4^m. Then, by following the same procedure to derive the sensitivity matrix presented in [29, Sec. III] and imitating [29, eq. (18)], we obtain the multiplication of $(\partial \mathbf{Z}/\partial x_l^m)$ and $\mathbf{e}_t$ in our multidomain problem

$$\left(\frac{\partial \mathbf{Z}}{\partial x_l^m}\mathbf{e}_t\right)_{s+p_i^m} = \sum_{j=1}^{4} \frac{\partial Z_{ii,pq}^{m,m}(i,j)}{\partial x_l^m} (\mathbf{e}_t)_{s+p_j^m}$$
$$= \sum_{j=1}^{4} \left\{ k_0^2 \sum_{k=1}^{9} \phi_i(\xi_k,\eta_k)\,\phi_j(\xi_k,\eta_k)\,|\mathbf{J}(\xi_k,\eta_k)|\, w_{k_\xi} w_{k_\eta} \right\} (\mathbf{e}_t)_{s+p_j^m} \tag{13}$$

where the column vector $\mathbf{e}_t$ is the solution of (1) when the whole inversion domain is illuminated by the tth transmitter; $s = \Sigma_{c=1}^{m-1}(N_i^c + 2N_b^c)$ denotes the index shift of the mth subdomain V_m with respect to $V_1, \ldots, V_{m-1}$; subscripts i and j of p_i^m and p_j^m take the values in the range of [1, 4] and denote the vertex indexes of one discrete element; subscripts i and j of ϕ_i and ϕ_j take the values in the range of [1, 4] and denote the indexes of the testing function and the basis function, respectively; subscript ii of $Z_{ii,pq}^{m,m}$ means that both the testing function and the basis function act on the internal nodes of V_m; and the definitions of ϕ_i, ϕ_j, ξ_k, η_k, $\mathbf{J}$, w_{k_ξ}, and w_{k_η} have been given in [29, Sec. III.A] and will not repeated here. Then, by referring to [29, eq. (14)], we use the adjoint solution $\mathbf{e}^*$ of (1) when the whole inversion domain is illuminated by the rth receiver to multiply $(\partial \mathbf{Z}/\partial x_l^m)\mathbf{e}_t$ in (13) and obtain the multidomain sensitivity matrix term for the lth quadrilateral element inside D_m

$$\frac{\partial F_{r,t}^{sct}}{\partial x_l^m} = -\sum_{i=1}^{4} \left[(\mathbf{e}^*)^T\right]_{r,s+p_i^m} \sum_{j=1}^{4}$$
$$\left\{ k_0^2 \sum_{k=1}^{9} \phi_i(\xi_k,\eta_k)\,\phi_j(\xi_k,\eta_k)\,|\mathbf{J}(\xi_k,\eta_k)|\, w_{k_\xi} w_{k_\eta} \right\} (\mathbf{e}_t)_{s+p_j^m} \tag{14}$$

where F^{sct} takes E_y^{sct}. Finally, we can follow the procedure given in [29, Sec. III.C] and simultaneously reconstruct the real relative permittivity and conductivity in multiple subdomains $D_1, \ldots, D_M$ using FEBI-LM. The aforementioned derivation indicates that the DD significantly lowers the costs of FEBI-LM in the reconstruction by only assembling the sensitivity submatrices for M subdomains instead of the whole domain and thus reducing the dimension of the final sensitivity matrix.

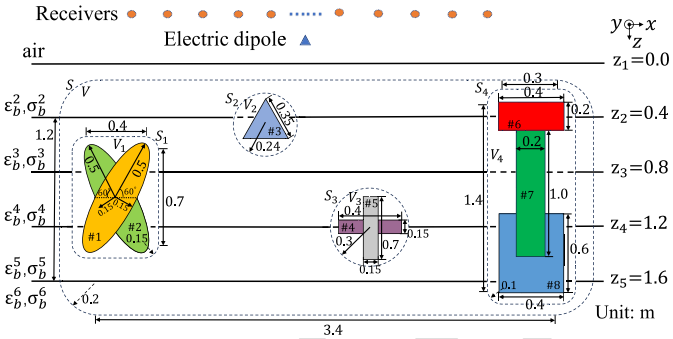

Fig. 2. Forward EM scattering model for multiple 2-D inhomogeneous scatterers straddling multiple subsurface layers. Geometry parameters of both the scatterers and the computational subdomains are annotated in the figure.

TABLE I

DIELECTRIC PARAMETERS AND CENTER COORDINATES OF EIGHT SCATTERER PARTS FOR THE SCATTERING MODEL SHOWN IN FIG. 2

Parameter \ Scatterer	#1	#2	#3	#4	#5	#6	#7	#8
ε	3.4	4.3	3.0	3.8	4.5	2.8	3.6	4.8
σ (mS/m)	3.0	3.5	5.0	6.0	5.5	2.5	4.5	4.0
center x coordinate (m)	−1.5	−1.5	−0.5	0.5	0.5	1.5	1.5	1.5
center z coordinate (m)	1.0	1.0	0.5	1.2	1.2	0.4	1.0	1.4

TABLE II

COMPARISONS OF DISCRETIZATION AND COMPUTATIONAL COST FOR THE SCATTERING MODEL SHOWN IN FIG. 2

	number of elements	number of arcs	LMDGF time	LMDGF memory	FEBI time	FEBI memory
with DD	242993	3278	33.8	0.5	11.6	6.7
w/o DD	1014934	4026	91.7	1.6	46.5	14.1

Remark: the unit of time is minute; the unit of memory is GB.

III. FORWARD VALIDATION

In this section, we prove the superiority of FEBI with DD over that without DD for the computation of EM scattering from multiple 2-D inhomogeneous scatterers straddling multiple subsurface layers. Fig. 2 shows the scattering configuration. The geometry parameters such as the layer boundary positions, the sizes of two overlapped tilted ellipses, the triangle, the cross-shape, and the rectangular piston, the sizes of the whole rounded rectangular domain V, the sizes of the rounded rectangular subdomains V_1 and V_4, and the sizes of the circular subdomains V_2 and V_3 are annotated in the figure. The relative permittivity values of the background layers are $\varepsilon_b^2 = 2.2$, $\varepsilon_b^3 = 1.6$, $\varepsilon_b^4 = 2.5$, $\varepsilon_b^5 = 1.3$, and $\varepsilon_b^6 = 3.0$. Their corresponding conductivity values are $\sigma_b^2 = 1.2$ mS/m, $\sigma_b^3 = 0.8$ mS/m, $\sigma_b^4 = 1.6$ mS/m, $\sigma_b^5 = 0.6$ mS/m, and $\sigma_b^6 = 2.0$ mS/m. The first layer is air. The dielectric parameters and center coordinates of eight parts of the four inhomogeneous scatterers are listed in Table I. Note that the center coordinates of the four subdomains V_1–V_4 are the same as those of scatterer parts #1, #3, #5, and #7, respectively. The center of the domain V is located at (0.0, 1.0) m. There is only one unit electric dipole located at (0.0, −0.2) m. By contrast, we evenly place 49 receivers on the horizontal line at $z = -0.5$ m. The coordinate of the first receiver is (−2.4, −0.5) m and the increment between two adjacent receivers

IEEE Proof

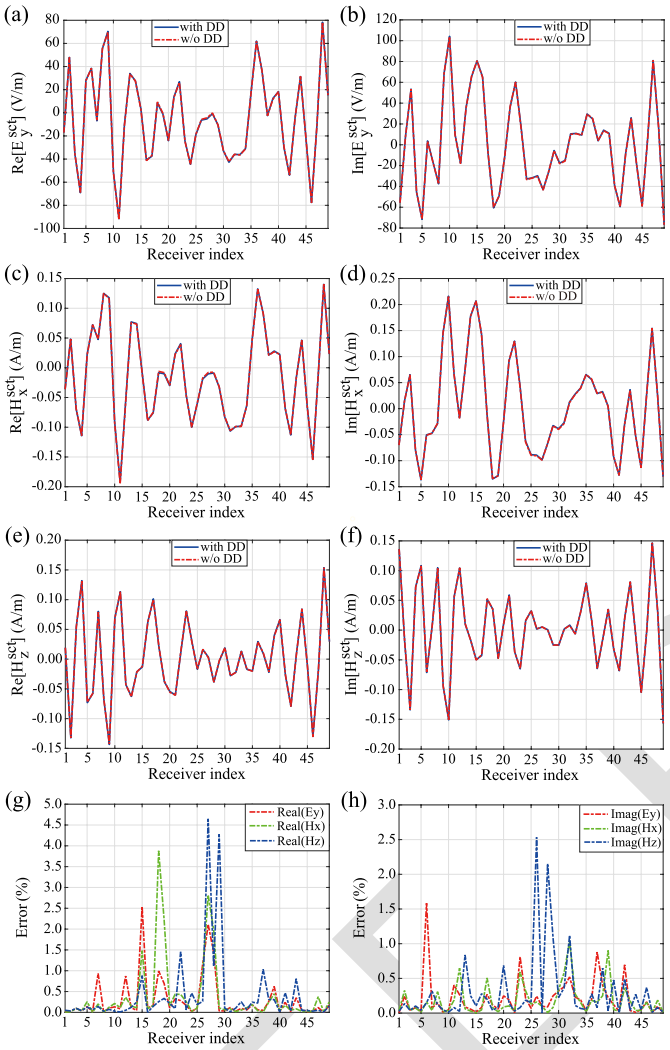

Fig. 3. Comparisons of the scattered EM fields at the receiver array computed by the FEBI method with and without DD. (a) Real part of E_y^{sct}. (b) Imaginary part of E_y^{sct}. (c) Real part of H_x^{sct}. (d) Imaginary part of H_x^{sct}. (e) Real part of H_z^{sct}. (f) Imaginary part of H_z^{sct}. (g) Relative errors of the real parts computed by FEBI with DD with respect to those computed by FEBI without DD. (h) Relative errors of the imaginary parts computed by FEBI with DD with respect to those computed by FEBI without DD.

is 0.1 m. The operation frequency is 1 GHz. The FEBI with DD is implemented in the four subdomains V_1–V_4, while that without DD is implemented in the domain V. All the numerical computation is performed on a workstation with a 48-core Intel Xeon 6248R 3.0 G CPU and 1024 GB of RAM. The discretization mesh information for the two methods is shown in the second and third columns of Table II.

Fig. 3 shows the comparisons of computed scattered fields at the receiver array by FEBI with DD and without DD and the relative errors among them. We can see that the results from the two methods match well. The mean relative errors of E_y^{sct}, H_x^{sct}, and H_z^{sct} computed by FEBI with DD with respect to those computed by FEBI without DD are 1.10%, 1.14%, and 1.02%, respectively. The individual errors versus receivers are also displayed in Fig. 3(g) and (h). Obviously, smaller scattered field values correspond to larger relative errors. The comparisons of the computational cost of FEBI with DD and without DD are listed in Table II. As can be seen, the cost for both the computation of LMDGFs and the implementation of FEBI is much lower when the DD is adopted than when the DD is not used. Indeed, as listed in Table II, both the discretized arcs on the boundaries and the quadrilateral elements inside the computational domains are significantly reduced when the DD is adopted. Consequently, the computational cost is also reduced thanks to the RBCs connecting multiple boundaries.

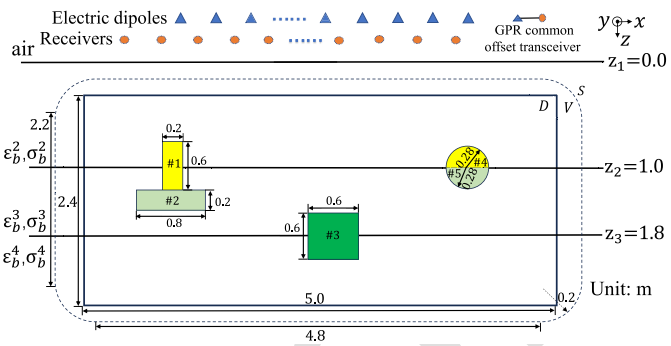

Fig. 4. EM reconstruction model for three 2-D inhomogeneous scatterers that straddle multiple subsurface layers and are placed far from each other. Geometry parameters of the scatterers are annotated in the figure.

IV. Reconstruction Assessment

In this section, we use two numerical cases to show the superiority of the FEBI-LM method with DD over that without DD for the reconstruction of multiple inhomogeneous objects straddling multiple subsurface layers. In the first case, we verify the feasibility and efficiency of the FRTM with level set and K-means clustering to determine the multiple domains and the FEBI-LM with DD to invert for permittivity and conductivity values of three inhomogeneous objects that are placed far from each other. In the second case, we test the algorithms for some harsh situations, e.g., the inversion data are contaminated by noise or scatterers are close to each other. In the FRTM, the common-offset GPR profiles are synthesized by the free software gprMax [37]. In both cases, the excitation source is a Ricker wavelet with a center frequency of 1.5 GHz. The source and receiver spectra are sampled from 20 MHz to 4 GHz with a frequency step of 20 MHz. The coefficient α in (8) is empirically set as 1.5. The threshold β in (11) is empirically set as 0.07 and the threshold γ in (12) is empirically set as 0.1. In the FWI, to avoid the so-called "inverse crime" [38], we employ the commercial software COMSOL using meshes different from those used in the FEBI solver to simulate scattered field data recorded at the receiver array.

A. Three Subsurface Scatterers Placed Far From Each Other

As shown in Fig. 4, three inhomogeneous scatterers placed far from each other straddle three subsurface layers. Their dielectric parameters and center coordinates are listed in Table III. The background layer boundary positions and the sizes of the inhomogeneous "T" shape, the homogeneous square, and the inhomogeneous sphere are annotated in the

IEEE Proof

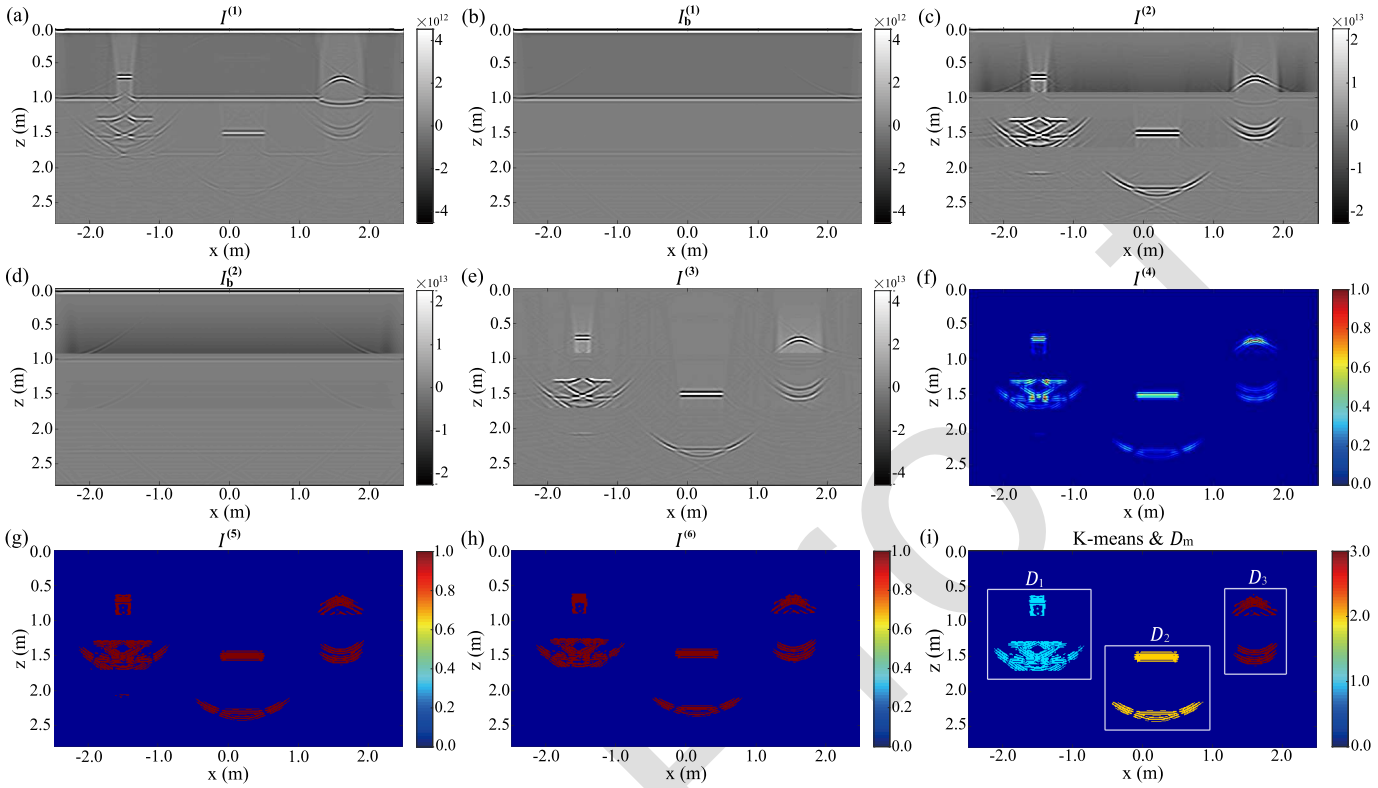

Fig. 5. Computed FRTM images for different algorithm steps listed in Section II-C. (a) Original image $I^{(1)}$ when the scatterers are present. (b) Original image $I_b^{(1)}$ of the layered background. (c) Compensated image $I^{(2)}$ when the scatterers are present. (d) Compensated image $I_b^{(2)}$ of the layered background. (e) Image $I^{(3)}$ for only the scatterers. (f) Normalized indicator function $I^{(4)}$. (g) Binary image $I^{(5)}$ with small clutters removed. (h) Binary image $I^{(6)}$ with large clutters removed. (i) K-means results and determined subdomains enclosed by white boxes.

TABLE III

DIELECTRIC PARAMETERS AND CENTER COORDINATES OF FIVE SCATTERER PARTS FOR THE RECONSTRUCTION MODEL IN FIG. 4

Parameter \ Scatterer	#1	#2	#3	#4	#5
ε	4.0	2.8	3.4	4.0	2.8
σ (mS/m)	7.0	13	10	7.0	13
center x coordinate (m)	−1.5	−1.5	0.2	1.6	1.6
center z coordinate (m)	1.0	1.4	1.8	0.86	1.14

figure. The dielectric parameters of the background layers are $\varepsilon_b^2 = 2.5$, $\sigma_b^2 = 3.0$ mS/m, $\varepsilon_b^3 = 1.8$, $\sigma_b^3 = 1.0$ mS/m, $\varepsilon_b^4 = 2.1$, and $\sigma_b^4 = 2.0$ mS/m. The FWI by FEBI-LM without DD is implemented in the rectangular region D shown in Fig. 4. The center of D is located at (0.0, 1.4) m. Unfortunately, the FWI by FEBI-LM with DD cannot be directly implemented since the location of each subsurface scatterer is unknown. Therefore, the FRTM with the level set to an indicator function and the K-means clustering discussed in Section II-C are employed to determine the inversion subdomain D_m for each scatterer in advance. The common-offset GPR profile used in the FRTM contains 1241 traces with a spatial step of 4 mm. The images generated by migration in different steps listed in Section II-C are displayed in Fig. 5.

We can see that FRTM only gives the approximate locations of subsurface scatterers, as shown in Fig. 5(a). The intensity of the image of the bottom square scatterer is weak due to the wave attenuation. This phenomenon is also obvious for the layered background image, as shown in Fig. 5(b). Fortunately, it can be compensated by the algorithm proposed in Section II-C and the results are shown in Fig. 5(c) and (d). Thanks to the compensation, the upper and lower boundaries of the three objects are clearly extracted, as shown in Fig. 5(e). This further guarantees the following operations to filter out the clutter and classify the pixels based on K-means, as shown in Fig. 5(f)–(i). The determined three subdomains are denoted by the white rectangular boxes D_1–D_3 and have the sizes of 1.4×1.12 m^2, 1.4×1.12 m^2, and 0.9×1.12 m^2, respectively, as shown in Fig. 5(i). Their center coordinates are (−1.5, 0.9) m, (0.1, 1.7) m, and (1.6, 0.9) m.

In order to perform FWI by FEBI-LM without DD in the region D and with DD in the subregions D_1–D_3, we evenly place 50 transmitters on the horizontal line at $z = -0.2$ m and 90 receivers on the horizontal line at $z = -0.1$ m. The coordinate of the first transmitter is (−9.8, −0.2) m and the increment between two adjacent transmitters is 0.4 m. The coordinate of the first receiver is (−17.8, −0.1) m and the increment between two adjacent receivers is 0.4 m. The operation frequency is 300 MHz. The structural consistency constraint (SCC) [23] is adopted to filter out the background clutter in FWI. The stop criterion of iterations is that the data misfit must be less than 5×10^{-3} and no "background" pixel is removed by the SCC algorithm in four consecutive steps. Fig. 6 shows the comparisons between the ground truth profiles and the reconstructed profiles without and with DD. We can see that no matter whether the DD has been applied to

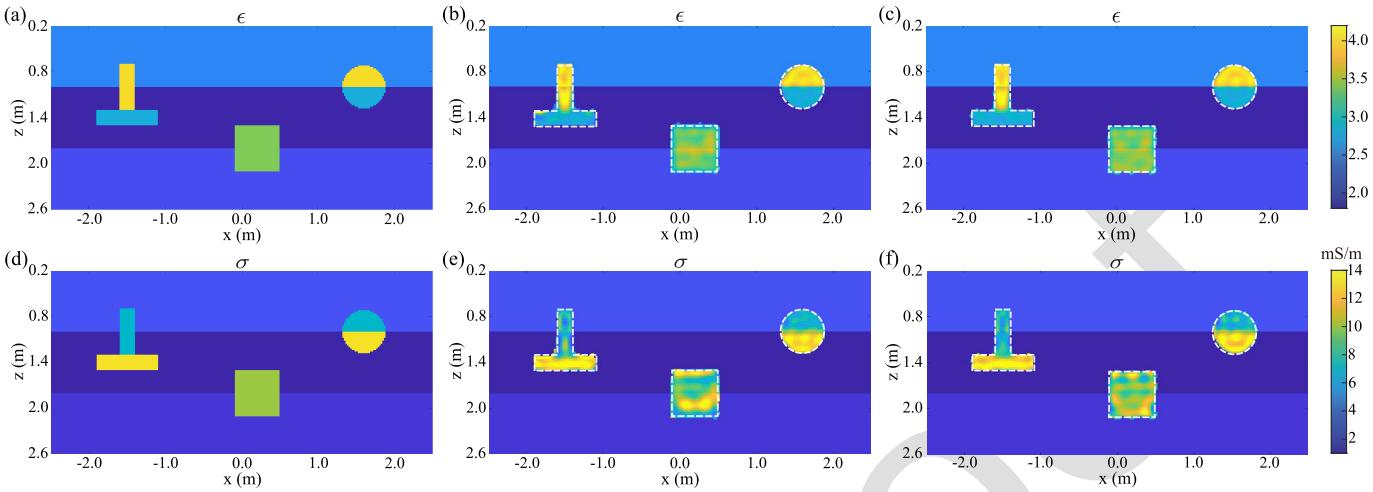

Fig. 6. Reconstructed profiles of the inhomogeneous "T" shape, the homogeneous square, and the inhomogeneous sphere straddling multiple subsurface layers. The first column shows the ground truth profiles. The second column shows the reconstructed profiles without DD applied. The third column shows the reconstructed profiles with DD applied. White dotted boxes denote true shapes.

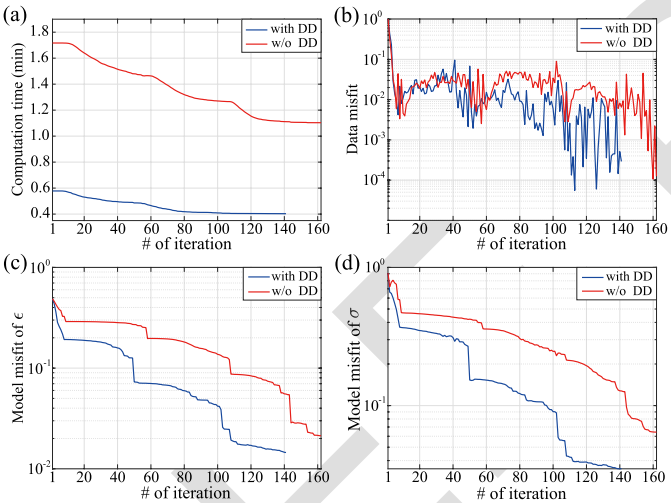

Fig. 7. Comparisons of (a) computation time, (b) data misfits of the scattered fields, (c) model misfits of ε, and (d) model misfits of σ in different FWI iteration steps with DD and without DD.

FEBI-LM or not, the reconstructed dielectric profiles are close to the true profiles. In order to further quantify the FWI performance by FEBI-LM, we use the model misfit and data misfit defined in [39, eq. (34)] and also record the peak memory consumption and time cost in the iterations. It is found that the FEBI-LM without DD needs 8.6 GB of peak memory, while that with DD only needs 3.0 GB of peak memory. Meanwhile, there is also a big discrepancy in each iteration step for the time consumption, as shown in Fig. 7(a). The total time to accomplish the FWI by FEBI-LM without DD is 219.8 min, while that is 64.7 min by FEBI-LM with DD. The FRTM takes 5.1 min and the total eight steps listed in Section II-C only take 9.8 s. This indicates that, once the FRTM is finished, the total time spent by the postprocessing algorithm to determine the boundaries of subdomains is negligible compared with the time spent by the following FWI. In addition, it should be emphasized that because the FRTM and the eight steps listed in Section II-C are only implemented once for the whole subsurface region, placing more subsurface scatterers will not increase their implementation time. The misfit curves shown in Fig. 7(b)–(d) verified the good inversion performance of FEBI-LM with and without DD and also confirmed the slightly better performance of FEBI-LM with DD compared to that without DD. All these results indicate that the FEBI-LM method with DD can achieve reliable reconstruction of multiple subsurface scatterers but with a rather low cost.

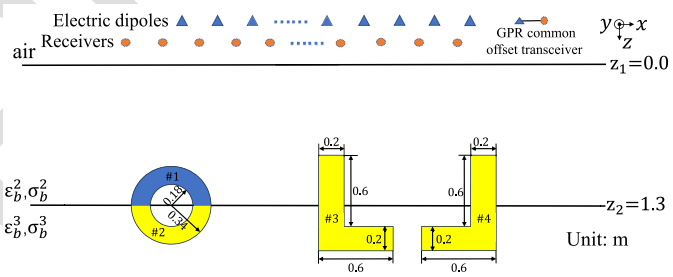

Fig. 8. EM reconstruction model for three 2-D scatterers that straddle two subsurface layers and are placed close to each other. Geometry parameters of the scatterers are annotated in the figure.

B. Three Subsurface Scatterers Placed Close to Each Other

As shown in Fig. 8, an inhomogeneous ring and two homogeneous "L" shapes placed close to each other straddle two subsurface layers. The dielectric parameters of the ring are $\varepsilon_s^1 = 2.5$, $\sigma_s^1 = 6.0$ mS/m, $\varepsilon_s^2 = 3.0$, and $\sigma_s^2 = 9.0$ mS/m. Two "L" shapes have the dielectric parameters $\varepsilon_s^3 = \varepsilon_s^4 = 3.0$ and $\sigma_s^3 = \sigma_s^4 = 9.0$ mS/m. The center of the ring is located at $(-1.2, 1.3)$ m. The center of the vertical bar of the left "L" shape is located at $(0.2, 1.3)$ m, while its horizontal-bar center is located at $(0.5, 1.6)$ m. The center of the vertical bar of the right "L" shape is located at $(1.4, 1.3)$ m, while its horizontal-bar center is located at $(1.1, 1.6)$ m. The background layer boundary positions and the sizes of three scatterers are annotated in the figure. The dielectric parameters of the background layers are $\varepsilon_b^2 = 1.5$, $\sigma_b^2 = 1.0$ mS/m, $\varepsilon_b^3 = 2.0$, and $\sigma_b^3 = 3.0$ mS/m.

IEEE Proof

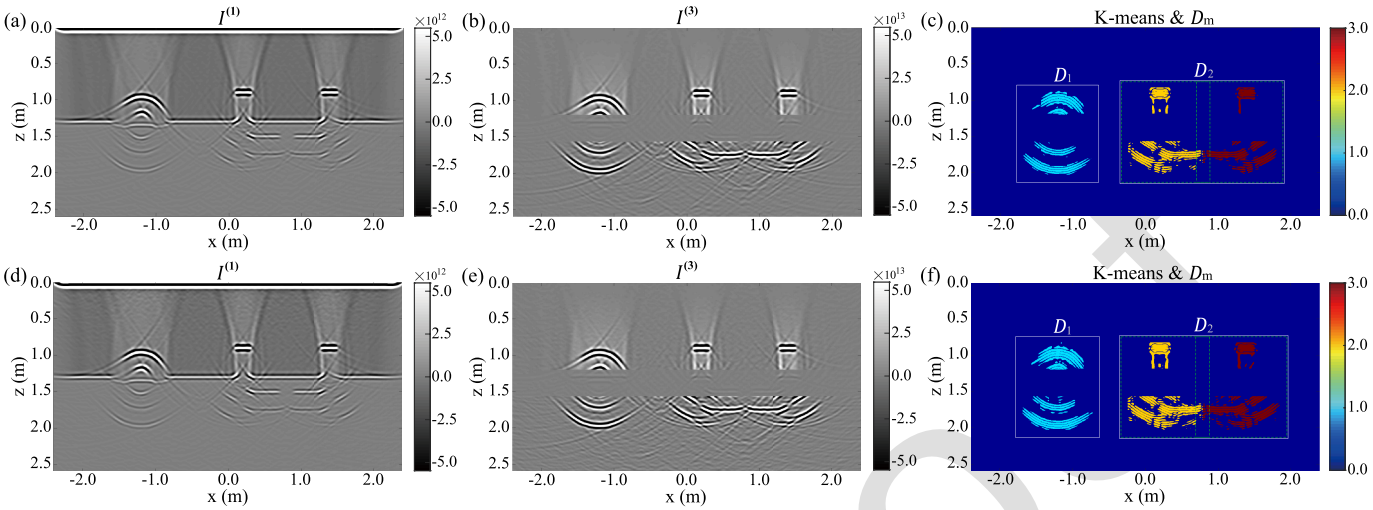

Fig. 9. Computed FRTM images for three representative steps listed in Section II-C when the GPR profiles are contaminated by noise. The first row shows the results when the 30 dB of noise is added. The second row shows the results when the 20 dB of noise is added. The third column shows the original image $I^{(1)}$. The second column shows the image $I^{(3)}$ for only the scatterers. The third column shows the K-means results and determined subdomains. The subdomains enclosed by dashed green lines are merged to form those enclosed by real white lines.

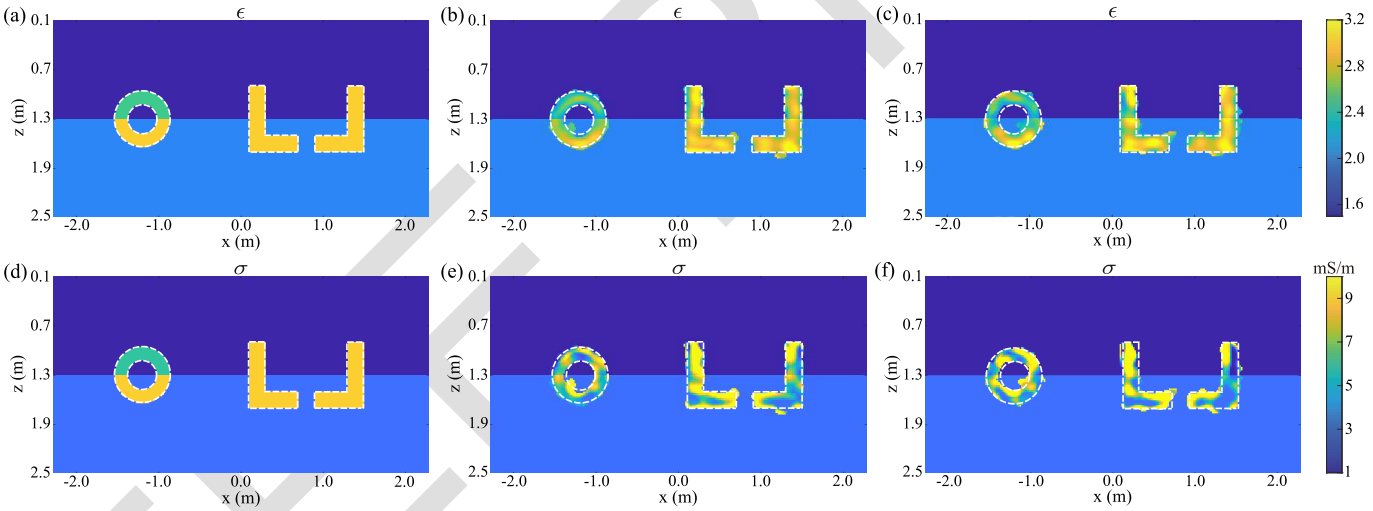

Fig. 10. Reconstructed profiles of the inhomogeneous ring and two homogeneous "L" shapes straddling two subsurface layers with DD applied. The first column shows the ground truth profiles. The second column shows the reconstructed profiles when the 30-dB noise is added. The third column shows the reconstructed profiles when the 20-dB noise is added. White dotted boxes denote true shapes.

In order to test the anti-noise ability of the FRTM with the level set and the K-means clustering discussed in Section II-C, we use 30 and 20 dB, respectively, of white Gaussian noise to contaminate the GPR data synthesized by the free software gprMax [37]. Here, the white Gaussian noise level is defined according to the signal-to-noise ratio (SNR) of power. The original FRTM images migrated from 1151 common-offset GPR traces with different noise levels are shown in Fig. 9(a) and (d). As can be seen, although the clutters caused by noise obviously show up in the images, the three objects are still clearly discernible. This is further verified by the compensated images only including scatterers and removing the layer effects, as shown in Fig. 9(b) and (e). We can see that the intensity of clutter caused by noise is much weaker than that of the scatterer. Therefore, even when the noise level is increased from 30 to 20 dB, the scatterer images have no obvious change. This means that the FRTM algorithm itself has certain anti-noise ability, which guarantees the following level set and K-means operations to determine the boundaries of the inversion subdomains. As shown in Fig. 9(c) and (f), the determined FWI subdomains are almost the same for two different noise levels. The only difference between the two subfigures is that there are more isolated "scatterer" pixels in Fig. 9(f) than in Fig. 9(c). This, of course, is caused by the larger noise but has no effect on the determined FWI subdomains. These observations imply that the algorithms proposed in Section II-C have a strong immunity to noise. On the other hand, it should be noted that the algorithms fail to distinguish the two "L" shapes, which have the nearest distance of $1.4\lambda_{\mathrm{FRTM}}$ although they can be empirically distinguished by our human being on the basis of images shown Fig. 9(b) and (e). Here, λ_{FRTM} is evaluated according to the 1.5-GHz center frequency of the Ricker wavelet and $\varepsilon_b^3 = 2.0$. Consequently, the two subdomains are

merged to form the final subdomain D_2, as shown in Fig. 9(c) and (f). By contrast, the subdomains D_1 and D_2 are not merged since the ring and the left "L" shape are placed $6.8\lambda_{\mathrm{FRTM}}$ from each other. These results indicate that the algorithms proposed in Section II-C may sometimes judge inaccurate subdomains due to the mutual interference of the images of two adjacent subsurface scatterers. Fortunately, the outline of an FRTM image is always larger than the true boundary of the scatterer and the determined subdomain boundary is further $0.5\lambda_{\mathrm{FRTM}}$ larger than the image outline. This guarantees that the determined inaccurate subdomain encloses the true scatterers, and they will be distinguished by the following FWI. In order to implement FEBI-LM with DD and SCC to accomplish FWI, we evenly place 70 transmitters on the horizontal line at $z = -0.2$ m and 110 receivers on the horizontal line at $z = -0.1$ m. The coordinate of the first transmitter is $(-13.8, -0.2)$ m and the increment between two adjacent transmitters is 0.4 m. The coordinate of the first receiver is $(-21.8, -0.1)$ m and the increment between two adjacent receivers is 0.4 m. The operation frequency is still 300 MHz. The simulated scattered field data are contaminated by 30 and 20 dB of white Gaussian noise. Fig. 10 shows the ground truth profiles, the FWI reconstructed profiles when 30 dB of noise is added, and the FWI reconstructed profiles when 20 dB of noise is added of the three subsurface scatterers. Three observations are made. First, the FEBI-LM with DD and SCC has a certain anti-noise ability in the inversion. When the 30 dB of noise is added, both the reconstructed shapes and dielectric parameter values are basically correct. In particular, the inhomogeneity of the ring clearly shows up in the reconstructed permittivity distribution, as shown in Fig. 10(b). Its model misfit is 4.0%. The reconstructed conductivity profile is worse and its model misfit is 17.2%. The inhomogeneity of the ring is not obvious, as shown in Fig. 10(e). This is because the imaginary part of the complex permittivity is much smaller than the real part, and thus, the scattered field data are not very sensitive to the conductivity variation compared with real permittivity. When we increase the noise level to 20 dB, although some obvious discontinuities of the permittivity and conductivity values appear inside the shapes, the reconstructed ring and "L" shapes are still discernible. The model misfits of the permittivity and conductivity become 6.1% and 26.7%, respectively. Second, the FEBI-LM with DD and SCC has a super-resolution in the FWI. The small gap between two "L" shapes is equal to $0.28\lambda_{\mathrm{FWI}}$, where $\lambda_{\mathrm{FWI}} = 5\lambda_{\mathrm{FRTM}}$. However, it is clearly identified by the FEBI-LM algorithm even when 20 dB of noise is added. This is because the FEBI-LM is a quantitative FWI method realized by strictly solving the EM scattering equation and the SCC can accurately locate the true boundary of a scatterer with a high probability [23]. Third, the FEBI-LM with DD consumes 3.2 GB of peak memory and 38.5 min to accomplish the FWI when 30 dB of noise is used to contaminate the scattered field data, while it consumes 3.2 GB of memory and 26.8 min when 20 dB of noise is added. We can see that the FEBI-LM can also efficiently reconstruct multiple subsurface scatterers, even when they are close to each other. In this situation, the DD may fail to distinguish adjacent subdomains, and they are merged in our algorithm, as shown in Fig. 9(f). However, the total area of the subdomains in which the FWI is implemented is still much smaller than that of the whole domain D. Consequently, the FEBI-LM with DD can also save a notable amount of computational resources.

V. Summary and Conclusion

In this work, we extend our previous work and introduce the DD into both the FEBI and the FEBI-LM methods to, respectively, lower the computation cost of EM forward scattering and quantitative reconstruction of multiple inhomogeneous scatterers straddling multiple subsurface planar layers. The RBCs are used to connect the multiple subdomains in the forward scattering computation accomplished by FEBI and the FRTM with the level set and the K-means clustering is used to determine the boundaries of multiple subdomains in FWI accomplished by FEBI-LM.

Three numerical experiments are carried out to justify the role of DD in lowering the computational cost of both the FEBI and FEBI-LM methods for EM scattering and subsurface reconstruction and also its feasibility in the hybrid reconstruction. It is found that the significantly lowered cost in the forward scattering FEBI computation is due to two reasons. The first one is that the total boundary length is decreased by DD. As a result, the computational cost of the LMDGFs is lowered. The second reason is that the total domain area is decreased by DD, and thus, the pure FEBI cost is lowered. These two aspects are also the major reasons for the low cost of the FWI implemented by LM since it iteratively calls the forward FEBI solver. On the other hand, by pushing the scattering scenarios to some harsh situations, we test the feasibility of FRTM with level set and K-means clustering to correctly locate the subdomains. It is found that the FRTM itself has a strong anti-noise ability. Its weakness lies in the low resolution of subsurface scatterers. Scatterers placed close to each other cannot be distinguished. Fortunately, this can be judiciously compensated by the following FWI implemented by FEBI-LM with DD and SCC as long as the subdomains of two close subsurface scatterers are merged.

One possible additional concern raised by readers is the influence of the dielectric parameters of the layered background medium, which may be unknown in the practical measurement. The conventional method is to use the echo signal model to retrieve the layer parameters at first [40]. However, it is not easy to distinguish echoes from layer boundaries and subsurface objects. Fortunately, the machine learning technique has been used to invert for layer dielectric parameters when noise signals from clutter exist [40] and may be used to invert for them even when echo signals from subsurface objects exist. However, this issue will be left as future work and not be discussed here.

Appendix

By referring to [29, eq. (5)], [39, eqs. (6)–(9)] with the duality theorem invoked, and [41, eqs. (5)–(9)], we can compute each element of the submatrices of $\mathbf{Z}^{m,m}$ and $\mathbf{Z}^{m,1}$ in (3) by

$$\mathbf{Z}^{m}_{uv}(p,q) =$$

IEEE Proof

$$\int_{D_m}\left[-\frac{1}{\mu_r}\left(\hat{y}\times\nabla_t\psi_p\right)\cdot\left(\hat{y}\times\nabla_t\psi_q\right)+k_0^2\epsilon_r\psi_p\psi_q\right]dxdz \quad \text{(A1a)}$$

$$\mathbf{Z}_S^m(p,q)=jk_0\int_{S_m}\psi_p\psi_q dt \quad \text{(A1b)}$$

$$\mathbf{Z}_M^{m,m}(p,q)=\frac{1}{2}\delta_{pq}-$$
$$⨍_{l_m^q}\left[G_{EM}^{yx}\left(\boldsymbol{\rho}_p^m,\boldsymbol{\rho}'\right)\hat{n}_z\left(\boldsymbol{\rho}'\right)-G_{EM}^{yz}\left(\boldsymbol{\rho}_p^m,\boldsymbol{\rho}'\right)\hat{n}_x\left(\boldsymbol{\rho}'\right)\right]dt' \quad \text{(A1c)}$$

$$\mathbf{Z}_J^{m,m}(p,q)=-\frac{1}{\eta_0}⨍_{l_m^q}G_{EJ}^{yy}\left(\boldsymbol{\rho}_p^m,\boldsymbol{\rho}'\right)dt' \quad \text{(A1d)}$$

$$\mathbf{Z}_M^{m,1}(p,q)=$$
$$-\int_{l_1^q}\left[G_{EM}^{yx}\left(\boldsymbol{\rho}_p^m,\boldsymbol{\rho}'\right)\hat{n}_z\left(\boldsymbol{\rho}'\right)-G_{EM}^{yz}\left(\boldsymbol{\rho}_p^m,\boldsymbol{\rho}'\right)\hat{n}_x\left(\boldsymbol{\rho}'\right)\right]dt' \quad \text{(A1e)}$$

$$\mathbf{Z}_J^{m,1}(p,q)=-\frac{1}{\eta_0}\int_{l_1^q}G_{EJ}^{yy}\left(\boldsymbol{\rho}_p^m,\boldsymbol{\rho}'\right)dt' \quad \text{(A1f)}$$

where ψ_p is the pth bilinear Lagrange polynomial testing function, ψ_q is the qth basis function, and $\nabla_t=\hat{x}(\partial/\partial x)+\hat{z}(\partial/\partial z)$ is the gradient operator in the xz plane. Subscripts u and v can take i or b, which indicates that the node is located inside or on the boundary of the subdomain D_m. δ_{pq} is the Kronecker symbol. $⨍$ is the Cauchy principal integral and l_m^q is the qth arc on the boundary S_m. $\boldsymbol{\rho}_p^m$ is the pth field point on the boundary S_m. n_x and n_z are the $\hat{x}$- and $\hat{z}$-components of the outward unit normal vector $\hat{n}$ on a certain boundary. G_{EM}^{yx}, G_{EM}^{yz}, and G_{EJ}^{yy} are certain components of the TE-mode LMDGFs, which can be directly obtained from the TM-mode ones given in [29, Appendix A] based on the duality theorem. In addition, it should be noted that both the integral and ∇_t applied to the basis or testing functions can only be implemented by transforming them to the reference-domain expressions, which have been given in [29, Appendix B].

The source matrix can be directly assembled by taking the incident field values at the field points on the boundary S_m

$$\mathbf{V}_S^m(p)=E_y^{inc}\left(\boldsymbol{\rho}_p^m\right) \quad \text{(A2)}$$

where p is the index of the testing function.

The radiation matrices are assembled by

$$\mathbf{R}_M^{E_y,m}(r,q)=$$
$$\int_{l_m^q}\left[G_{EM}^{yx}\left(\boldsymbol{\rho}_r,\boldsymbol{\rho}'\right)\hat{n}_z\left(\boldsymbol{\rho}'\right)-G_{EM}^{yz}\left(\boldsymbol{\rho}_r,\boldsymbol{\rho}'\right)\hat{n}_x\left(\boldsymbol{\rho}'\right)\right]dt' \quad \text{(A3a)}$$

$$\mathbf{R}_J^{E_y,m}(r,q)=\frac{1}{\eta_0}\int_{l_m^q}G_{EJ}^{yy}\left(\boldsymbol{\rho}_r,\boldsymbol{\rho}'\right)dt' \quad \text{(A3b)}$$

$$\mathbf{R}_M^{H_x,m}(r,q)=$$
$$\int_{l_m^q}\left[G_{HM}^{xx}\left(\boldsymbol{\rho}_r,\boldsymbol{\rho}'\right)\hat{n}_z\left(\boldsymbol{\rho}'\right)-G_{HM}^{xz}\left(\boldsymbol{\rho}_r,\boldsymbol{\rho}'\right)\hat{n}_x\left(\boldsymbol{\rho}'\right)\right]dt' \quad \text{(A3c)}$$

$$\mathbf{R}_J^{H_x,m}(r,q)=\frac{1}{\eta_0}\int_{l_m^q}G_{EJ}^{xy}\left(\boldsymbol{\rho}_r,\boldsymbol{\rho}'\right)dt' \quad \text{(A3d)}$$

$$\mathbf{R}_M^{H_z,m}(r,q)=$$
$$\int_{l_m^q}\left[G_{HM}^{zx}\left(\boldsymbol{\rho}_r,\boldsymbol{\rho}'\right)\hat{n}_z\left(\boldsymbol{\rho}'\right)-G_{HM}^{zz}\left(\boldsymbol{\rho}_r,\boldsymbol{\rho}'\right)\hat{n}_x\left(\boldsymbol{\rho}'\right)\right]dt' \quad \text{(A3e)}$$

$$\mathbf{R}_J^{H_z,m}(r,q)=\frac{1}{\eta_0}\int_{l_m^q}G_{HJ}^{zy}\left(\boldsymbol{\rho}_r,\boldsymbol{\rho}'\right)dt' \quad \text{(A3f)}$$

where r is the receiver index.

References

[1] P. Gao and L. M. Collins, "A theoretical performance analysis and simulation of time-domain EMI sensor data for land mine detection," *IEEE Trans. Geosci. Remote Sens.*, vol. 38, no. 4, pp. 2042–2055, Jul. 2000.

[2] H. Liu, X. Huang, F. Han, J. Cui, B. F. Spencer, and X. Xie, "Hybrid polarimetric GPR calibration and elongated object orientation estimation," *IEEE J. Sel. Topics Appl. Earth Observ. Remote Sens.*, vol. 12, no. 7, pp. 2080–2087, Jul. 2019.

[3] J. Zhang et al., "Quantitative crack depth monitoring based on traveling wave at millimeter-wave frequency," *IEEE Trans. Antennas Propag.*, vol. 70, no. 9, pp. 8321–8329, Sep. 2022.

[4] H. P. Huang and I. J. Won, "Characterization of UXO-like targets using broadband electromagnetic induction sensors," *IEEE Trans. Geosci. Remote Sens.*, vol. 41, no. 3, pp. 652–663, Mar. 2003.

[5] Y. Deng and X. Liu, "Electromagnetic imaging methods for nondestructive evaluation applications," *Sensors*, vol. 11, no. 12, pp. 11774–11808, Dec. 2011.

[6] S. Sun, "Qualitative and quantitative imaging in electromagnetic inverse scattering theory," Ph.D. thesis, Delft Univ. Technol., Delft, The Netherlands, 2017.

[7] J. Zhu and L. R. Lines, "Comparison of Kirchhoff and reverse-time migration methods with applications to prestack depth imaging of complex structures," *Geophysics*, vol. 63, no. 4, pp. 1166–1176, 1998.

[8] C. J. Leuschen and R. G. Plumb, "A matched-filter-based reverse-time migration algorithm for ground-penetrating radar data," *IEEE Trans. Geosci. Remote Sens.*, vol. 39, no. 5, pp. 929–936, May 2001.

[9] M. Wang, H. Wang, and H. Liu, "3D pre-stack reverse time migration of ground penetrating radar for subsurface imaging," in *Proc. 17th Int. Conf. Ground Penetrating Radar (GPR)*, Rapperswil, Switzerland, Jun. 2018, pp. 1–4.

[10] H. Liu, Z. Long, F. Han, G. Fang, and Q. H. Liu, "Frequency-domain reverse-time migration of ground penetrating radar based on layered medium Green's functions," *IEEE J. Sel. Topics Appl. Earth Observ. Remote Sens.*, vol. 11, no. 8, pp. 2957–2965, Aug. 2018.

[11] D. Colton, H. Haddar, and M. Piana, "The linear sampling method in inverse electromagnetic scattering theory," *Inverse Problems*, vol. 19, no. 6, pp. S105–S137, Nov. 2003.

[12] I. Catapano, L. Crocco, and T. Isernia, "On simple methods for shape reconstruction of unknown scatterers," *IEEE Trans. Antennas Propag.*, vol. 55, no. 5, pp. 1431–1436, May 2007.

[13] A. J. Devaney, "Geophysical diffraction tomography," *IEEE Trans. Geosci. Remote Sens.*, vol. GE-22, no. 1, pp. 3–13, Jan. 1984.

[14] K. Ren and R. J. Burkholder, "A uniform diffraction tomographic imaging algorithm for near-field microwave scanning through stratified media," *IEEE Trans. Antennas Propag.*, vol. 64, no. 12, pp. 5198–5207, Dec. 2016.

[15] K. Belkebir, P. C. Chaumet, and A. Sentenac, "Superresolution in total internal reflection tomography," *J. Opt. Soc. Amer. A, Opt. Image Sci.*, vol. 22, no. 9, pp. 1889–1897, Sep. 2005.

[16] Z. Wei and X. Chen, "Deep-learning schemes for full-wave nonlinear inverse scattering problems," *IEEE Trans. Geosci. Remote Sens.*, vol. 57, no. 4, pp. 1849–1860, Apr. 2019.

[17] M. Zhong, Y. Chen, J. Li, and F. Han, "Reconstruction of subsurface objects by LSM and FWI from limited-aperture electromagnetic data," *IEEE Trans. Geosci. Remote Sens.*, vol. 60, 2022, Art. no. 2003011.

[18] C. Dong, Y. Jin, M. Ferrara, and K. Priddy, "A study of multistatic ultrasonic tomography using propagation and back-propagation method," in *Algorithms for Synthetic Aperture Radar Imagery XVIII* (International Society for Optical Engineering), vol. 8051. Bellingham, WA, USA: SPIE, May 2011, Art. no. 805106.

[19] W. C. Chew, *Waves and Fields in Inhomogeneous Media*. New York, NY, USA: IEEE Press, 1995, ch. 9.

[20] P. Zwamborn and P. M. van den Berg, "The three dimensional weak form of the conjugate gradient FFT method for solving scattering problems," *IEEE Trans. Microw. Theory Techn.*, vol. 40, no. 9, pp. 1757–1766, Sep. 1992.

[21] F. Han, J. Zhuo, N. Liu, Y. Liu, H. Liu, and Q. H. Liu, "Fast solution of electromagnetic scattering for 3-D inhomogeneous anisotropic objects embedded in layered uniaxial media by the BCGS-FFT method," *IEEE Trans. Antennas Propag.*, vol. 67, no. 3, pp. 1748–1759, Mar. 2019.

[22] L.-P. Song, Q. Huo Liu, F. Li, and Z. Qing Zhang, "Reconstruction of three-dimensional objects in layered media: Numerical experiments," *IEEE Trans. Antennas Propag.*, vol. 53, no. 4, pp. 1556–1561, Apr. 2005.

IEEE Proof

[23] J. Zhuo, L. Ye, F. Han, L. Xiong, and Q. H. Liu, "Multiparametric electromagnetic inversion of 3-D biaxial anisotropic objects embedded in layered uniaxial media using VBIM enhanced by structural consistency constraint," *IEEE Trans. Antennas Propag.*, vol. 68, no. 6, pp. 4774–4785, Jun. 2020.

[24] R. Huang, Q. Wu, and F. Han, "3-D EM scattering and inverse scattering by anisotropic objects straddling multiple planar uniaxial layers with a 2-D locally rough surface," *IEEE Trans. Antennas Propag.*, vol. 71, no. 11, pp. 8936–8948, Nov. 2023.

[25] R. Gholami and V. Okhmatovski, "Surface–volume–surface EFIE formulation for fast direct solution of scattering problems on general 3-D composite metal–dielectric objects," *IEEE Trans. Antennas Propag.*, vol. 68, no. 7, pp. 5742–5747, Jul. 2020.

[26] S. Chaillat, L. Desiderio, and P. Ciarlet, "Theory and implementation of $\mathcal{H}$-matrix based iterative and direct solvers for Helmholtz and elastodynamic oscillatory kernels," *J. Comput. Phys.*, vol. 351, pp. 165–186, Dec. 2017.

[27] S. Omar and D. Jiao, "A linear complexity direct volume integral equation solver for full-wave 3-D circuit extraction in inhomogeneous materials," *IEEE Trans. Microw. Theory Techn.*, vol. 63, no. 3, pp. 897–912, Mar. 2015.

[28] Z. Long, H. Cai, X. Hu, G. Li, and O. Shao, "Parallelized 3-D CSEM inversion with secondary field formulation and hexahedral mesh," *IEEE Trans. Geosci. Remote Sens.*, vol. 58, no. 10, pp. 6812–6822, Oct. 2020.

[29] J. Li, Z. Li, R. Huang, and F. Han, "Electromagnetic FWI of 2-D inhomogeneous objects straddling multiple planar layers by finite-element boundary integral and Levenberg–Marquardt methods," *IEEE Trans. Geosci. Remote Sens.*, vol. 63, 2025, Art. no. 2001012.

[30] K. Zhao, M. N. Vouvakis, and J.-F. Lee, "The adaptive cross approximation algorithm for accelerated method of moments computations of EMC problems," *IEEE Trans. Electromagn. Compat.*, vol. 47, no. 4, pp. 763–773, Nov. 2005.

[31] H. Liu, Z. Deng, F. Han, Y. Xia, Q. H. Liu, and M. Sato, "Time-frequency analysis of air-coupled GPR data for identification of delamination between pavement layers," *Construct. Building Mater.*, vol. 154, pp. 1207–1215, Nov. 2017.

[32] K. A. Michalski and J. R. Mosig, "Multilayered media Green's functions in integral equation formulations," *IEEE Trans. Antennas Propag.*, vol. 45, no. 3, pp. 508–519, Mar. 1997.

[33] F. Han, J. Zhuo, S. Lu, J. Wang, and Q. H. Liu, "Explicit semianalytical expressions of sensitivity matrices for the reconstruction of 1-D planarly layered TI media illuminated by 3-D sources," *IEEE Trans. Antennas Propag.*, vol. 70, no. 2, pp. 1547–1552, Feb. 2022.

[34] M. Rabbani, A. Tavakoli, and M. Dehmollaian, "A hybrid quantitative method for inverse scattering of multiple dielectric objects," *IEEE Trans. Antennas Propag.*, vol. 64, no. 3, pp. 977–987, Mar. 2016.

[35] A. M. Ikotun, A. E. Ezugwu, L. Abualigah, B. Abuhaija, and J. Heming, "K-means clustering algorithms: A comprehensive review, variants analysis, and advances in the era of big data," *Inf. Sci.*, vol. 622, pp. 178–210, Apr. 2023.

[36] C. A. Balanis, *Advanced Engineering Electromagnetics*. New York, NY, USA: Wiley, 2012, p. 968.

[37] C. Warren, A. Giannopoulos, and I. Giannakis, "gprMax: Open source software to simulate electromagnetic wave propagation for ground penetrating radar," *Comput. Phys. Commun.*, vol. 209, pp. 163–170, Dec. 2016.

[38] A. Wirgin, "The inverse crime," Oct. 2018, *arXiv:math-ph/0401050*.

[39] J. Li, Z. Li, Z. Guan, and F. Han, "2-D electromagnetic scattering and inverse scattering from anisotropic objects under TE illumination solved by the hybrid SIM/SEM," *IEEE Trans. Antennas Propag.*, vol. 72, no. 4, pp. 3517–3528, Apr. 2024.

[40] X. Yang et al., "Layered media parameter inversion method based on deconvolution autoencoder and self-attention mechanism using GPR data," *IEEE Trans. Geosci. Remote Sens.*, vol. 62, 2024, Art. no. 4501714.

[41] J. Li, Z. Guan, J. Wang, L.-Y. Xiao, and Q. H. Liu, "Contracting electromagnetic full-wave inversion of 2-D inhomogeneous objects with irregular shapes based on the hybrid SESI forward solver," *IEEE Trans. Geosci. Remote Sens.*, vol. 60, 2022, Art. no. 5305411.

Jiawen Li received the B.S. degree in electronic science and technology from Wuhan University of Technology, Wuhan, China, in 2011, and the Ph.D. degree in electromagnetic field and microwave technology from Xiamen University, Xiamen, China, in 2023.

Since August 2023, he has been with Guangxi Normal University, Guilin, China, where he is currently an Assistant Professor with the School of Electronic and Information Engineering. His research interests include electromagnetic scattering and inverse scattering in complex media and the full-wave inversion (FWI) of anisotropic targets.

Qi Qiang Liu (Member, IEEE) received the Ph.D. degree in electromagnetic field and microwave technology from Xiamen University, Xiamen, China, in 2023.

Since August 2023, he has been with Hangzhou Dianzi University, Hangzhou, China, where he is currently an Assistant Professor with the School of Electronics and Information Engineering. His research interests include numerical methods for multiphysics and multiscale coupling in electromagnetics, heat transfer, and mechanics.

Zhen Guan received the Ph.D. degree in computational science from the School of Mathematical Sciences and the Institute of Electromagnetics and Acoustics, Xiamen University, Xiamen, China, in 2022.

During her Ph.D. degree, she joined the doctoral program at the Mathematical Institute of the Department of Mathematics and Computer Science, Free University of Berlin, Berlin, Germany. From July 2022 to July 2024, she was an Assistant Professor with the School of Science, Tianjin University of Technology, Tianjin, China. Since August 2024, she has been a Post-Doctoral Fellow under a joint appointment between Great Bay University, Dongguan, Guangdong, China, and the University of Science and Technology of China, Hefei, China. Her research interests include fast algorithms for computational electromagnetics and inverse scattering problems and their applications in engineering.

Feng Han (Senior Member, IEEE) received the B.S. degree in electronic science from Beijing Normal University, Beijing, China, in 2003, the M.S. degree in geophysics from Peking University, Beijing, in 2006, and the Ph.D. degree in electrical engineering from Duke University, Durham, NC, USA, in 2011.

From 2011 to 2015, he was a Software Engineer at Wavenovation, Inc., Xiamen, China. In July 2015, he joined the Institute of Electromagnetics and Acoustics, Xiamen University, Xiamen, China, as an Assistant Professor and was promoted to an Associate Professor in 2020. In October 2023, he joined the School of Computing and Information Technology, Great Bay University, Guangdong, China, as an Associate Professor. He has published over 60 articles in refereed journals. His research interests include electromagnetic scattering and inverse scattering in complex media, multiparametric and multidimensional hybrid electromagnetic full-wave inversion (FWI), fast electromagnetic FWI based on machine learning, configuration of the antenna array for electromagnetic inverse problems, and geophysical electromagnetic exploration and inversion.

IEEE Proof